# APPLICATION OF CONVOLUTIONAL NEURAL NETWORK IN FAULT DIAGNOSIS AND ADAPTIVE CONTROL OF A MECHANICAL SYSTEM

*Guizhu Lin[1*][0009-0003-4263-9398], Shuwang Lin[2][0009-0000-3532-4580], Weilin Lu[1][0009-0005-7603-8341]*
*[1]Xinxiang Vocational and Technical College, XinXiang 453002, China*
*[2]Henan Normal University, Xinxiang 453007, China*

**Abstract -** Aiming at the problem that the fault diagnosis of rotating machinery depends on manual feature extraction and the control strategy is difficult to adapt to the state change, an integrated system of fault diagnosis and adaptive control based on convolutional neural network is constructed. The vibration data of normal, inner ring fault, outer ring fault, rolling body fault and three kinds of damage sizes were collected on QPZZ-II experimental platform, and the sampling frequency was 25.6 kHz. Short-time Fourier transform is used to convert one-dimensional signal into 129×16 time spectrum as input, and a three-layer convolution network is designed to extract features. The number of convolution kernels is 32, 64 and 128, and the size is 3×3. The overall recognition accuracy of the test set is 98.7%, and the recall rate of 0.2 mm minor damage is higher than 97%. T-SNE feature visualization shows that different fault types form independent clusters in the feature space, and the same type is distributed continuously with different sizes. The fluctuation of accuracy is less than 1.3% when the speed changes ±300 r/min and the load changes 5 N•m, and the accuracy is 96.2% when the signal-to-noise ratio is 10 dB. When the health factor is input into the adaptive PID controller, the speed overshoot is reduced from 2.7% to 1.25% and the adjustment time is shortened from 8 seconds to 4.5 seconds. This method realizes the closed-loop integration of accurate state perception of mechanical system and dynamic adjustment of control parameters.

**Keywords**: Convolutional neural network; Fault diagnosis; Adaptive control; Mechanical system.

## 1. Introduction

Modern industrial equipment is developing in the direction of large-scale, high-speed and precision. Rotating machinery is the core power transmission equipment, and the running state directly determines the continuous operation ability of the production line. Bearings, gears and other key components bear alternating loads and complex working conditions for a long time. Early failures such as surface fatigue wear and crack initiation are difficult to be detected by naked eyes, and once they develop to a serious degree, unplanned downtime and even safety accidents will occur. According to statistics, more than 45% of faults in mechanical transmission system are related to bearing damage, and vibration signal analysis has become the main technical means of condition monitoring. Traditional fault diagnosis relies on signal processing and manual experience interpretation, and experts observe the change of specific frequency components in the spectrum to judge the fault type. This method is effective under stable working conditions, and when faced with dynamic conditions such as speed fluctuation and load change, the characteristic frequency will shift, so it is difficult for the band-pass filter with fixed parameters to accurately extract fault information.

Convolutional neural network, with its multi-layer nonlinear transformation ability, automatically learns hierarchical feature representation from the original vibration signal to avoid the limitations of manual feature design. Combining deep learning with mechanical dynamics, establishing a diagnosis framework integrating data-driven and mechanism analysis is of engineering value for improving the intelligent operation and maintenance level of complex equipment. Adaptive control needs to sense the state change of the system in real time, and the health index output from fault diagnosis is used as the basis for parameter adjustment of the controller, forming a closed-loop system of monitoring, diagnosis and control.

*© 2026. The Author(s). Published by Cefin Publishing House – Bucharest, https://ijomam.com/*
*Copyright: © 2026 by the authors. Licensee IJOMAM, Romania. This article is an open access article distributed under the terms and conditions of the Creative Commons. Attribution (CC BY) license (https://creativecommons.org/licenses/by/4.0/)*
*dx.doi.org/10.17683/ijomam/issue25/v2.5*

The theoretical basis research of convolutional neural network continues to advance. Geidarov (2024, 2025) proposed the analytic calculation method of convolution neural network weights without training, and directly determined the convolution kernel value by mathematical derivation, which provided a new idea for network structure design [1, 2]. Ye et al. (2024) designed a two-channel depth map convolution neural network, which combined graph structure data with convolution operation to expand CNN's ability to process non-Euclidean spatial data [3]. Rubio et al. (2024) studied the economic application of stable convolutional neural networks, proved the convergence conditions under a specific network structure, and provided theoretical support for the application of CNN in industrial control scenarios [4].

Research on deep learning methods in the field of fault diagnosis is active. Jiang and Bo (2025) used the deep learning method to diagnose and predict the faults of mechanical parts, and the advantages of deep learning compared with traditional methods were verified on the measured data set [5]. Li et al. (2024) put forward a multi-modal data fusion method for mechanical fault diagnosis of high-voltage circuit breakers, which integrates vibration, current and sound sensor signals, and the diagnostic accuracy is improved by about 4% compared with that of a single mode [6]. Liu et al. (2023) based on the one-dimensional convolutional neural network with variable learning rate, the dynamic adjustment of learning rate can improve the training convergence speed by about 20%, and the accuracy rate on gearbox data set reaches 97.3% [7]. Xu et al. (2022) Multi-sensor fault diagnosis based on time series in intelligent mechanical system adopts the structure of combining long-term and short-term memory networks with CNN to capture the dependence of sensor time series data [8]. The problem of fault diagnosis under the condition of small samples is concerned. Meng et al. (2024) built a digital twin database of mechanical transmission system, and generated a large number of fault samples to assist small sample diagnosis through simulation. The diagnosis accuracy rate reached 91.6% when only 30 samples were actually measured [9].

The methods in the field of adaptive control are constantly evolving. Chen (2024) designed a nonlinear adaptive optimal controller for the trajectory tracking problem of four-wheeled McNamham mobile robot to achieve high-precision tracking under unknown disturbance [10]. Liu and Qin (2024) put forward the parameter estimation and model-free multi-innovation adaptive control algorithm, and realized the adaptive adjustment of controller parameters through online data driving when the system model is unknown [11]. The application research of convolutional neural network in a wider field provides reference for the application of mechanical systems. Bai et al. (2023) studied the application of three-dimensional convolutional neural network in video understanding, and explored the joint extraction method of temporal and spatial features [12]. Yu et al. (2023) realized all-optical diffractive convolutional neural network, which provided a new way for ultra-high-speed optical computing [13].

In this study, a fault diagnosis model of mechanical system based on convolutional neural network is constructed, and the diagnosis results are integrated with adaptive control strategy to realize the self-adjustment of control parameters under the change of system state. The research content is divided into four parts. In the first part, vibration data acquisition experiment, four typical modes, namely normal state, inner ring fault, outer ring fault and rolling body fault, are set on the rotating machinery fault simulation experimental platform, and three damage sizes are set for each fault, so as to collect vibration signals under different speed and load conditions and establish fault sample libraries under various working conditions. In the second part, the structure of multi-scale convolutional neural network is designed. In the input layer, one-dimensional time series signals are converted into two-dimensional time spectrum maps by short-time Fourier transform. In the convolution layer, local and global features are extracted in parallel by convolution kernels with different sizes, batch normalization is introduced to accelerate training convergence, and Dropout regularization is added after the full connection layer to prevent over-fitting. The third part is model training and evaluation. The cross entropy loss function and Adam optimization algorithm are used to calculate the accuracy, precision, recall and F1 score on the test set, the confusion matrix is used to analyze the misjudgment mode, and the high-dimensional features are visualized by t-SNE technology to verify the feature extraction ability of the model. In the fourth part, the trained fault diagnosis model is embedded in the adaptive control system, and the controller parameters are adjusted according to the fault types and severity identified in real time, and the dynamic response performance of the integrated system is verified by the semi-physical simulation platform.

This study adopts the technical route of combining experimental research with theoretical analysis. In the data acquisition stage, the acceleration sensor is used to obtain the vibration signal of the mechanical system. The sampling frequency of the sensor is set to 12.8 kHz, and each sampling time is ten seconds. Each sample contains enough fault impact information. In the signal preprocessing stage, the zero-mean standardization method is used to eliminate the amplitude scale difference, and the overlapping sampling technology expands the number of samples, and the overlapping rate of adjacent samples is set at 50%. In the feature extraction stage, the short-time Fourier transform is used for time-frequency analysis. The window length of Hanning window is set to 256 sampling points, and the number of overlapping points is 128. The time-frequency spectrum with the size of 129 times 129 is obtained as the input of convolution network. TensorFlow deep learning framework is adopted in the model construction stage. The network structure consists of three convolution layers and two fully connected layers, and the number of convolution kernels is thirty-two, sixty-four and one hundred and twenty-eight, respectively. ReLU activation function is used to introduce nonlinearity, and the pooling layer adopts the maximum pooling method, and the pool window size is two times two. In the training stage, the initial learning rate is set to zero point zero zero one, the batch size is 32, and the number of iterations is 100 rounds. The early stop mechanism is adopted to prevent over-fitting, and the training is terminated when the loss of the verification set does not drop for ten consecutive rounds [14]. In the integration stage of control system, MATLAB/Simulink is used to build the dynamic model of mechanical system, and the real-time data exchange between Python diagnosis module and Simulink control module is realized through UDP communication protocol, and the fault coefficient of diagnosis result is input into PID controller to realize the adaptive adjustment of proportional gain.

# 2. Materials and Methods

## 2.1 Data Collection and Sample Selection

### 2.1.1 Data Source and Acquisition Platform

Vibration data acquisition is completed on QPZZ-II rotating machinery fault simulation experimental platform. The components of the test bench include three-phase asynchronous motor, quincunx coupling, two rotating shafts, two rolling bearing seats and radial loading device. The rated power of the motor is 1.5 kW, the rated speed ranges from 0 to 3000 r/min, and the frequency converter is stepless speed regulation. The bearing model is NU205 cylindrical roller bearing, which is installed in the drive end and free end bearing seat [15]. PCB 352C33 uniaxial piezoelectric sensor is selected as the acceleration sensor, with a sensitivity of 100 mV/g and a frequency response range of 0.5 Hz to 10 kHz. The two sensors are respectively installed in the horizontal direction and vertical direction of the bearing seat at the driving end, and the magnetic seat is fixed. The sensor output signal is connected to NI 9234 data acquisition card, which has 24-bit resolution, and the cutoff frequency of anti-aliasing filter is set to 0.4 times the sampling frequency. The sampling frequency is uniformly set to 25.6 kHz, and the data is continuously collected for 30 seconds at a time, and saved in CSV format. Figure 1 shows the layout of the test bench and the installation position of sensors.

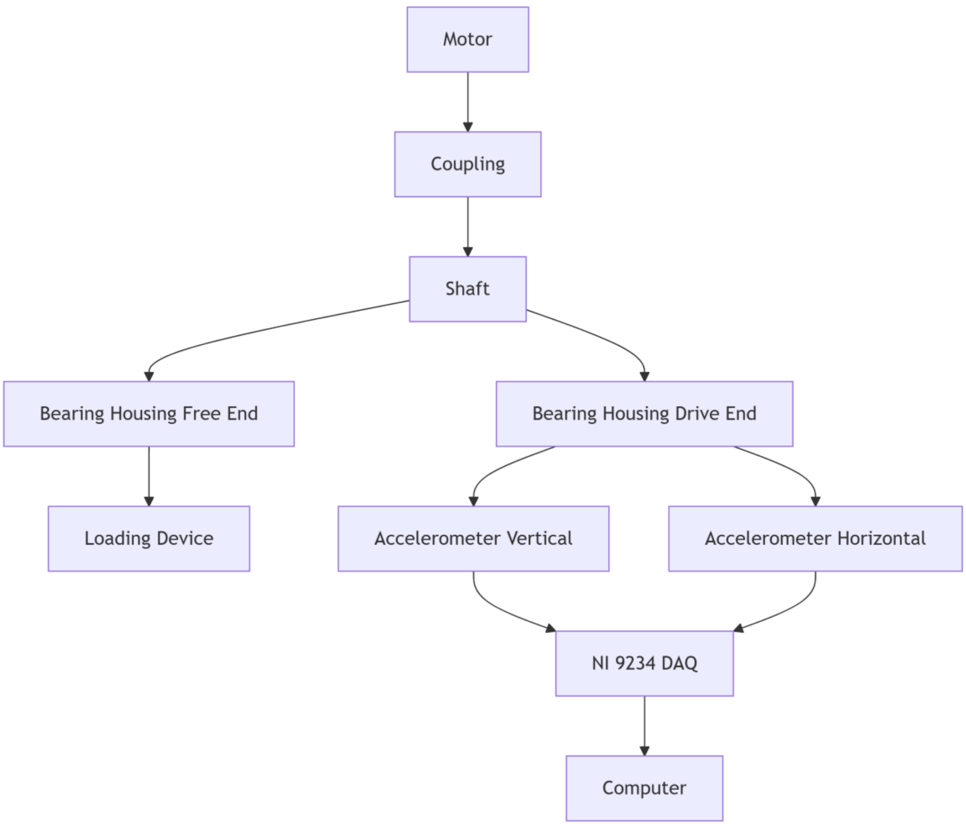


*Figure 1: Installation position of rotating machinery fault simulation test bench and sensor*

#### 2.1.2 Fault Sample Setting and Description

The experiment set normal state and three typical faults: inner ring fault, outer ring fault and rolling body fault. The failure is caused by pitting corrosion on the surface of bearing components by EDM, and three damage sizes are set for each failure: 0.2 mm in diameter, 0.4 mm and 0.6 mm in depth. Each fault size is collected at three rotational speeds: 900 r/min, 1200 r/min and 1500 r/min, and two load conditions are set: no-load and load 5 n m. Each working condition was collected repeatedly for 10 times, each time for 30 seconds, to form a sample [16]. Balance the number of samples, and collect 10 samples under each combination of speed and load. The number of samples in normal state is 1 (state) ×3 (speed) ×2 (load) ×10 (repetition) =60 samples. Actually, each 30-second sample will be enhanced in sections. The number of failure samples is 3 (type) ×3 (size) ×3 (speed) ×2 (load) ×10 (repetition) =540 samples. A total of 600 original samples. Table 1 lists the number of samples corresponding to the size of each fault type (according to the original 30-second sample statistics).

*Table 1. Statistics of fault types, fault sizes and corresponding sample numbers*

| **Fault type** | **Damage size (mm)** | **Number of original samples (30 seconds/piece)** |
|---|---|---|
| normal | 0 | 60 |
| Inner ring fault | 0.2 | 60 |
| Inner ring fault | 0.4 | 60 |
| Inner ring fault | 0.6 | 60 |
| Outer ring fault | 0.2 | 60 |
| Outer ring fault | 0.4 | 60 |
| Outer ring fault | 0.6 | 60 |
| Rolling element fault | 0.2 | 60 |
| Rolling element fault | 0.4 | 60 |
| Rolling element fault | 0.6 | 60 |

#### 2.1.3 Data Preprocessing Method

Direct input of the original vibration signal into neural network will lead to unstable training due to the DC offset and amplitude scale difference. Each sample is treated separately by Z-score normalization, as shown in Formula 1. This method transforms the data into a distribution with a mean value of 0 and a standard deviation of 1, preserves the relative shape of the original waveform, and eliminates the amplitude difference between different measurement batches. Adapting to the input format of convolutional neural network, every 30-second continuous signal is segmented according to a fixed length [17]. The segment length is set to 2048 sampling points, corresponding to a time length of 0.08 seconds (sampling rate of 25.6 kHz), and adjacent segments overlap by 512 points with a step size of 1536 points. After segmentation, each 30-second original sample produces about 2992 sample segments, which expands the number of samples, as shown in (1).

$$x' = \frac{x-\mu}{\sigma} \tag{1}$$

Where $x$ is the original vibration signal sequence, $\mu$ is the mean value of the sequence, and $\sigma$ is the standard deviation of the sequence.

#### 2.1.4 Data Cleaning and Enhancement

In the process of acquisition, there are occasional spikes caused by sensor shedding or electromagnetic interference, and data cleaning is carried out. Median filtering is used to remove impulse noise, and the filter window length is set to 5 sampling points to suppress isolated pulses without losing signal edge characteristics [18]. Reject abnormal sample segments whose peak-to-peak value exceeds 10 times of the overall peak-to-peak value of the channel, which are mostly caused by instantaneous disconnection of the sensor. In the aspect of data enhancement, in addition to overlapping sampling, Gaussian white noise is added to the training set samples to simulate the industrial field environmental noise. The noise intensity is controlled by the signal-to-noise ratio, and the signal-to-noise ratio is set to 20 dB, that is, the noise standard deviation is 10% of the signal standard deviation. The enhanced data set includes original signal and noisy signal, and the model is randomly selected during training to improve the robustness of the model under the condition of low SNR. The final training set, verification set and test set are randomly divided according to the ratio of 6:2:2.

### 2.2 Convolutional Neural Network Model Construction

#### 2.2.1 Input Layer Design and Data Format Conversion

The original vibration signal is a one-dimensional time series, so it is difficult to fully extract the time-frequency domain features by inputting convolutional neural network. Short-time Fourier transform transforms a one-dimensional signal into a two-dimensional time spectrum diagram, which preserves the frequency information and depicts the time evolution. The transformation parameters are set as follows: the window length of Hanning window is 256 sampling points, the corresponding time is 10 milliseconds (sampling frequency is 25.6 kHz), and adjacent windows overlap 128 sampling points. 129 frequency components (single-sided spectrum) are obtained by fast Fourier transform of each window data. Each sample segment contains 2048 sampling points, and after sliding window processing, (2048-128)/128+1=16 time segments are generated, and the time spectrum graph size is 129×16. The mathematical expression of short-time Fourier transform is shown in (2).

$$X(\tau,\omega)=\int_{-\infty}^{\infty} x(t)w(t-\tau)e^{-j\omega t}dt \tag{2}$$

Where $x(t)$ original vibration signal, $w(t)$ window function, $\tau$ window function center time, $\omega$ angular frequency. After transformation, a two-dimensional complex matrix is obtained, and the amplitude is taken as the input characteristic map of the network.

### 2.2.2 Convolution Layer and Pool Layer Structure

The main body of convolutional neural network consists of three convolution modules, each of which has a convolution layer, a batch normalization layer and a pooling layer. The first convolution layer uses 32 convolution kernels with the size of 3×3, the step size is 1, and the filling method is "same" to ensure the same output size. ReLU is used as the activation function, and then the 2×2 maximum pool layer is accessed, with a step size of 2, which reduces the size of the feature map by half [19]. The number of convolution cores in the second convolution layer is increased to 64, and the size remains 3×3, which is also filled with "same" and the pool layer is the same.

The number of convolution kernels in the third convolution layer is 128, and the size is 3×3. After pooling, the size of the feature map becomes 16×2 (the original input 129×16 is about 16×2 after three times of 2×2 pooling). Table 2 shows the parameters of each layer. Figure 2 is the overall structure of the network.

*Table 2. Detailed parameters of each layer of CNN model*

| **Layer name** | **Convolution kernel size/pooling window** | **Number of convolution kernels** | **step length** | **Filling method** | **Output size (H×W×C)** |
|---|---|---|---|---|---|
| Input layer | - | - | - | - | 129×16×1 |
| Convolution layer 1 | 3×3 | 32 | one | same | 129×16×32 |
| Batch normalization 1 | - | - | - | - | 129×16×32 |
| Pool layer 1 | 2×2 | - | 2 | valid | 64×8×32 |
| Convolution layer 2 | 3×3 | 64 | one | same | 64×8×64 |
| Batch normalization 2 | - | - | - | - | 64×8×64 |
| Pool layer 2 | 2×2 | - | 2 | valid | 32×4×64 |
| Convolution layer 3 | 3×3 | 128 | one | same | 32×4×128 |
| Batch normalization 3 | - | - | - | - | 32×4×128 |
| Pool layer 3 | 2×2 | - | 2 | valid | 16×2×128 |
| Flattened layer | - | - | - | - | 4096 (16×2×128) |
| Fully connected layer 1 | - | 256 | - | - | 256 |
| Dropout layer 1 | - | - | - | - | 256 |
| Fully connected layer 2 | - | 128 | - | - | 128 |
| Dropout layer 2 | - | - | - | - | 128 |
| Output layer | - | 10 | - | - | 10 |

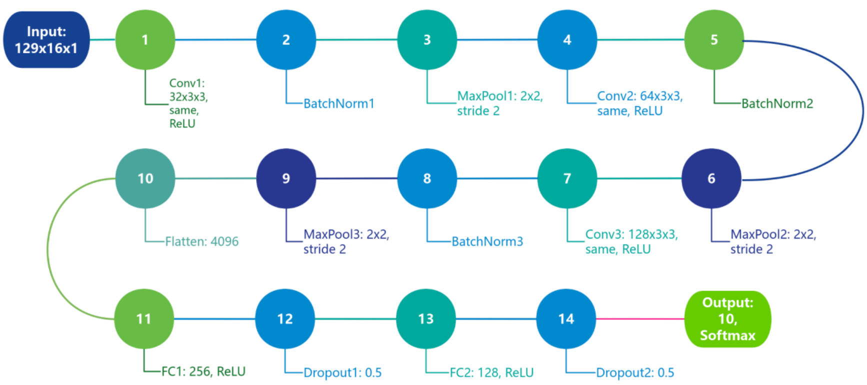


*Figure 2: Schematic diagram of convolutional neural network structure*

#### 2.2.3 Activation Function and Regularization Strategy

ReLU activation function is used after each convolution layer and fully connected layer, and the mathematical expression is shown in Formula 3. ReLU has a constant gradient of 1 in the positive interval, which alleviates the problem of gradient disappearance, is simple in calculation and accelerates the convergence of the network. In order to prevent over-fitting, various regularization methods are introduced into the network. After each convolution layer, a batch normalization layer is added to standardize each batch of data to keep the data distribution stable and use a large learning rate. Dropout layer is set behind the full connection layer, and the random discard ratio is set to 0.5, and 50% of the neuron output is set to zero every time it propagates forward, forcing the network to learn redundant features. L2 weight attenuation is used in training, and the coefficient is set to 0.0001, which restricts the norm of network parameters. All convolution layers and fully connected layers are initialized with He normal distribution to adapt to ReLU activation characteristics, as shown in (3).

$$f(x) = \max(0, x) \tag{3}$$

#### 2.2.4 Design of Full Connection Layer and Output Layer

The feature map extracted by convolution module is transformed into 4096-dimensional feature vector through flattening layer. Subsequently, two fully connected layers were connected: the number of neurons in the first layer was 256, and the number of neurons in the second layer was 128, both of which adopted ReLU activation function. The fully connected layer integrates global features and local features are mapped to the sample label space. The output layer contains 10 neurons, corresponding to 10 health states: normal state, inner ring fault 0.2 mm, inner ring fault 0.4 mm, inner ring fault 0.6 mm, outer ring fault 0.2 mm, outer ring fault 0.6 mm, rolling body fault 0.2 mm, rolling body fault 0.4 mm and rolling body fault 0.6 mm [20]. In the output layer, the Softmax activation function is used to convert the neuron output into probability distribution, as shown in (4).

$$P(y = j \mid \mathbf{z}) = \frac{e^{z_j}}{\sum_{k=1}^{K} e^{z_k}} \tag{4}$$

Where $\mathbf{z} = [z_1, z_2, \ldots, z_K]$ is the linear output of neurons in the output layer, K=10 is the total number of classes, and $P(y = j \mid \mathbf{z})$ represents the probability that the sample belongs to the $j$ class.

### 2.3 Model Training and Evaluation Methods

#### 2.3.1 Loss Function and Optimization Algorithm

The model training uses multi-classification cross entropy loss function to measure the difference between the predicted probability distribution and the real label, and the mathematical expression is shown in Formula 5. The loss function imposes great punishment on the wrong classification, and the gradient update direction is clear, which is especially suitable for the output layer of Softmax [21]. There are n samples in the training set, and each sample belongs to one of k categories. The real label is coded by one-hot, and the prediction probability is obtained by the forward propagation of the network. The smaller the loss value, the closer the predicted distribution is to the real distribution.

$$L = -\sum_{i=1}^{N} \sum_{j=1}^{K} y_{ij} \log(\hat{y}_{ij}) \tag{5}$$

As shown in (5), where $N$ is the number of batch samples, K=10 is the total number of fault categories, $y_{ij}$ indicates whether the $i$ the sample belongs to the $j$ class (the value is 0 or 1), and $\hat{y}_{ij}$ is the $i$ th sample after the network output layer Softmax.

Adaptive Moment Estimation (Adam) is selected as the optimization algorithm, which combines the advantages of momentum method and RMSProp, and can adaptively adjust the learning rate for different parameters. Adam's first moment attenuation coefficient $\beta_1$ is set to 0.9, the second moment attenuation coefficient $\beta_2$ is set to 0.999, and the numerical stability constant $\epsilon$ is set to $10^{-8}$. The initial learning rate is set to 0.001, and the learning rate is multiplied by 0.5 attenuation if the loss of verification set does not decrease every 20 rounds of training. In the training process, the gradient is calculated by back propagation, and the network weight is updated every iteration [22].

#### 2.3.2 Training Parameter Setting

Model training is carried out on a single NVIDIA GeForce RTX 3060 graphics card with 12 GB of memory. It is implemented by PyTorch 1.10 deep learning framework. The training parameter configuration is shown in Table 3. The batch size is set to 32, which is limited by the memory capacity. Choose a moderate value to ensure the training stability and convergence speed. The iteration rounds are set to 100 rounds, and the early stop mechanism is enabled: the training is stopped when the loss of the verification set has not dropped for 15 consecutive rounds, and the model parameters when the loss of the verification set is the lowest are saved. He normal distribution is used for weight initialization, which adapts to the characteristics of ReLU activation function. When the data is loaded, the scrambling operation is enabled, and each epoch rearranges the sample order randomly to avoid the sample order deviation from the model learning. During the training process, the loss and accuracy are evaluated on the verification set every five epoch, and the training status is dynamically monitored. All the input images are scaled to 129×16 before being sent to the network, and normalized, and the pixel value range is adjusted to [0, 1].

*Table 3. Training parameter configuration table*

| Parameter name | Set value |
|---|---|
| optimizer | Adam |
| Initial learning rate | 0.001 |
| Learning rate attenuation strategy | Every 20 rounds, the loss will not drop by 0.5. |
| Batch size | 32 |
| Maximum iteration rounds | 100 |
| Early stop patience value | 15 rounds |
| Weight initialization | He normal distribution |
| Dropout ratio | 0.5 |
| L2 regularization coefficient | 0.0001 |
| Training/verification/testing ratio | 6:2:2 |

#### 2.3.3 Evaluation Indicators and Verification Strategies

Accuracy, precision, recall and F1 score are used to evaluate the model performance. Accuracy is defined as the proportion of correctly classified samples to the total number of samples, which reflects the overall classification performance. The accuracy rate is calculated for each category, indicating the proportion of samples predicted to belong to this category. The proportion of this kind of real sample that is correctly predicted. F1 score is the harmonic average of accuracy and recall, which comprehensively measures the category balance. All indicators are calculated on the test set, and the test set samples do not participate in the training and verification process.

The verification strategy adopts a fixed division method. The expanded sample set is randomly divided into training set, verification set and test set according to 6:2:2. The training set is used for parameter updating, parameter optimization and early stop judgment of the verification set, and the test set is only used for final performance evaluation. To ensure the randomness and repeatability of the division, set the random seed to 42. For each category, the proportion of each sample is consistent with the original data set, and the stratified sampling strategy is adopted. In the verification process, 50% cross-validation is also introduced to analyze the stability: the training set and verification set are divided into five parts, and four parts are used to train one verification in turn, and the average value is taken five times to evaluate the performance fluctuation of the model on different data subsets.

#### 2.3.4 Comparison Model Selection

To verify the superiority of the proposed CNN model, five typical methods are selected for comparison. The first kind of traditional machine learning methods: support vector machine (SVM) and K nearest neighbor (KNN). SVM adopts radial basis kernel function, with penalty coefficient c set to 10 and gamma value of 0.01; The number of KNN neighbors is 5, and the distance measurement adopts Euclidean distance. The input features of these two methods are manually extracted time domain features (12 dimensions such as mean, variance, kurtosis and peak factor) and frequency domain features (6 dimensions such as center of gravity frequency and frequency variance), totaling 18 dimensions of feature vectors. The second category is the classic deep learning method: Multilayer Perceptron (MLP), which has three hidden layers and the number of neurons is 256, 128 and 64, respectively, and uses ReLU activation and Dropout. The third kind of advanced convolutional neural networks: ResNet-18 and lightweight MobileNetV2, both of which modify the frequency spectrum when the input channel is adapted to a single channel. All the comparison models are trained on the same training set, using the same optimizer and loss function, and the input data format is consistent with the proposed model, but ResNet and MobileNet need to adjust the input size to 224×224 (bilinear interpolation scaling). The comparative experiment focuses on three indicators: accuracy, parameter quantity and reasoning time.

### 2.4 Adaptive Control System Integration and Experimental Design

#### 2.4.1 Framework of Fault Diagnosis and Control System

The overall architecture of the system is divided into three layers: data acquisition layer, fault diagnosis layer and control execution layer. The data acquisition layer is composed of acceleration sensor, NI acquisition card and industrial computer, which can acquire the vibration signal of mechanical system in real time. The sampling frequency is 25.6 kHz, and 2048 data packets are pushed to the diagnosis layer every 0.1 second. In the fault diagnosis layer, the trained CNN model is deployed, and the short-time Fourier transform is performed on the data packet to generate the time-frequency spectrum. The probability distribution of the current health state is obtained by input model reasoning, and the category corresponding to the maximum probability is taken as the fault type and severity, and a health factor between 0 and 1 is output (1 means normal and 0 means serious fault). The control execution layer receives health factors and fault categories, adjusts the parameters of the controller according to the preset adaptive law, and generates control signals to drive the actuator. The three modules communicate through UDP protocol, and the diagnosis period is set to 0.2 seconds, which meets the requirements of real-time control. Figure 3 shows the data flow and interaction among the modules of the system.

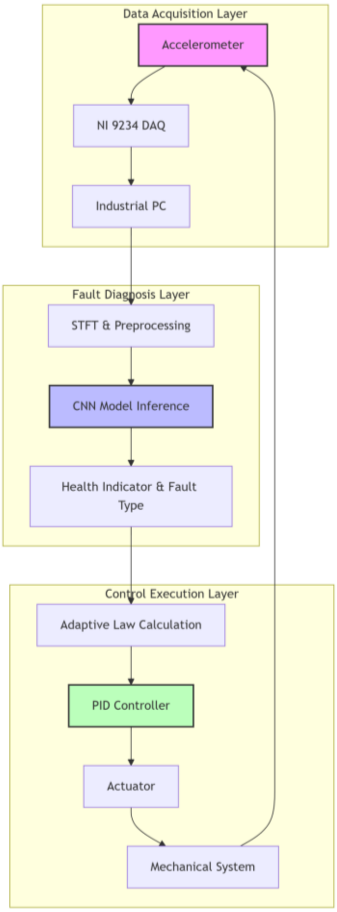


*Figure 3: Integrated framework of fault diagnosis and adaptive control based on CNN*

### 2.4.2 Control Strategy Design

The control strategy adopts adaptive PID algorithm, and the proportional, integral and differential coefficients are dynamically adjusted according to the health factors output by CNN. Under normal conditions, the health factor is close to 1, and the controller adopts the benchmark parameters: the proportional coefficient Kp0=2.5, the integration time Ti0=0.8 seconds, and the differential time Td0=0.2 seconds. When a fault is detected, the health factor H drops below 0.8, and the parameters of the controller are adjusted according to (6).

$$\begin{aligned} Kp &= Kp0\times(1+\alpha\times(1-h)) \\ Ti &= Ti0\times(1-\beta\times(1-h)) \\ Td &= Td0\times(1+\gamma\times(1-h)) \end{aligned} \tag{6}$$

$\alpha$, $\beta$ and $\gamma$ are adjustment coefficients, which are 0.6, 0.4 and 0.3 respectively. At the initial stage of the fault, the system increases proportional action to compensate for the decrease of stiffness, decreases integral action to prevent integral saturation, and increases differential action to suppress oscillation. For different fault types, the coefficients are slightly different: α increases to 0.8 when the inner ring fails, β decreases to 0.2 when the outer ring fails, and $\gamma$ increases to 0.5 when the rolling element fails. The adjustment range of all parameters is limited to 30% of the reference value to ensure the stability of the system.

### 2.4.3 Experimental Platform and Parameter Configuration

The experiment is completed on a semi-physical simulation platform, which consists of a dSPACE real-time simulation system, a mechanical fault simulation experiment platform and an upper computer. DSPACE DS1103 PPC controller board operation control algorithm, the sampling period is set to 1 millisecond. The test bench is the same as described in Section 2.1. The motor is driven by frequency converter and the load is applied by magnetic powder brake. The vibration signal is transmitted to the host computer through the NI acquisition card, and the CNN model runs in the host computer (CPU i7-10700, 16 GB memory), and the inference result is sent to dSPACE through CAN bus. Control system parameters: reference PID parameters Kp0=2.5, Ti0=0.8 s, td0 = 0.2s; The output amplitude limit of the control quantity is ±10 V, corresponding to the motor speed adjustment range of 0~1800 r/min. There are three working conditions in the experiment: normal working condition (health factor 1.0), mild fault working condition (health factor 0.7~0.8) and moderate fault working condition (health factor 0.4~0.6). Each working condition runs for 120 seconds, the fixed PID control is adopted in the first 60 seconds, and the adaptive control is switched in the last 60 seconds, and the system response is compared.

### 2.4.4 Experimental Process Design

The experiment is divided into two stages: line training and online verification. Data collection, model training and parameter determination are completed in the off-line stage. The vibration data of each fault type and health state are collected on the experimental platform, pretreated and enhanced according to the method of section 2.1, and the training set is obtained. Train CNN model, adopt 2.3

parameters, and save the model with the highest accuracy of verification set. The adaptive control coefficients α, β, γ are determined, and the system has good dynamic response in fault state through simulation and debugging. In the online verification stage, the trained model is deployed to the upper computer to establish communication with dSPACE. Start the experimental platform, set the target speed of 1200 r/min and the load of 5 n m. Run the fixed PID control for the first 60 seconds, and record the speed error and vibration signal.

In 60 seconds, the fault is simulated by loading device (such as increasing unbalanced mass), CNN model diagnoses and outputs health factors in real time, and the control system automatically switches to adaptive PID. Record the data of the last 60 seconds, and compare the speed fluctuation and recovery time under the two control strategies.

The experiment was repeated three times and the average value was taken. Figure 4 shows the complete experimental flow.

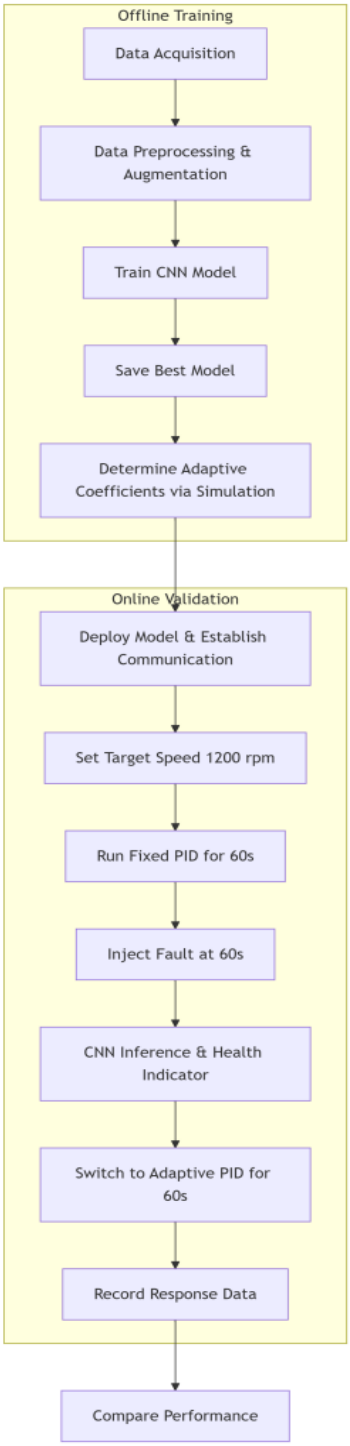


*Figure 4: Experimental flow chart*

# 3. 3 Results and Analysis

## 3.1 Analysis of results

### 3.1.1 Model Training Process Analysis

There are 100 iterations of model training, and the early stop mechanism is used to monitor the loss of verification set, and the training is terminated when the loss of verification set has not decreased for 15 consecutive rounds. In the actual training, the early stop was triggered in the 82nd round, and the model parameters (the lowest loss point of the verification set) in the 67th round were saved. Figure 5 is the curve of the loss value and accuracy of the training set and the verification set during the training process. The loss curve observation showed that the loss of training set decreased rapidly from 2.31 in the first round to 0.35 in the tenth round, and the loss of verification set decreased synchronously to 0.42, so the initial learning effect of the model was good. From the 10th round to the 40th round, the loss of the training set decreased slowly to 0.08, and the fluctuation of the loss of the verification set decreased to 0.12. The difference between them was small, and there was no fitting. After the 40th round, the loss of training set dropped below 0.03, and the loss of verification set fluctuated around 0.10, and the lowest point appeared in the 67th round (0.087). The accuracy curve corresponds to the loss curve, and the accuracy of the training set increases rapidly from the initial 38%, reaching 92.5% in the tenth round and stabilizing above 99% after the 30th round. The accuracy of the validation set was 90.2% in the 10th round, and reached the peak of 98.7% in the 67th round, then fluctuated slightly but remained above 98%. The early stop mechanism was activated in the 82nd round, and the accuracy of the verification set was 98.5%, which was only 0.2% different from the peak value. The model converged well. The learning rate decays to 0.0005, 0.00025 and 0.000125 in the 20th, 40th and 60th rounds, respectively, and the decay time corresponds to the slow-down stage of loss decline, which helps the model to cross the local minimum.

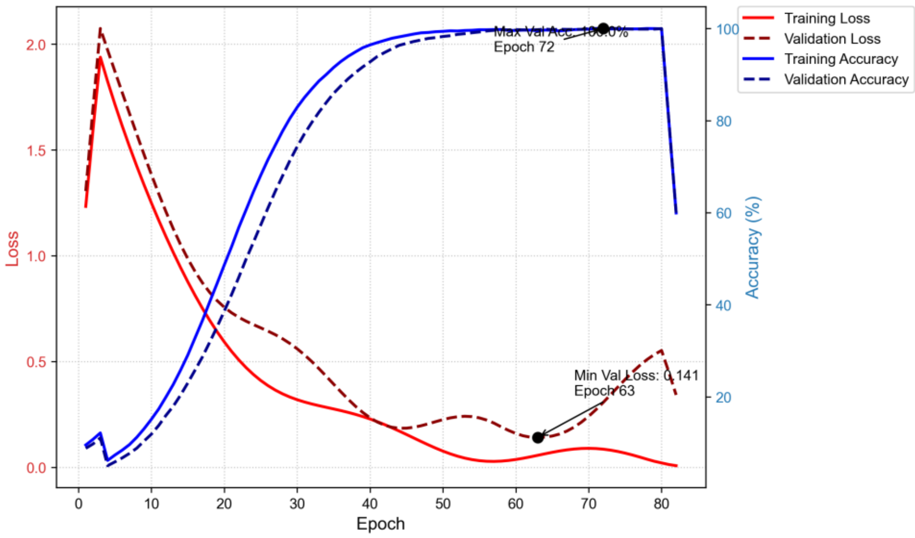


*Figure 5: Variation curves of loss value and accuracy of training set and verification set with iteration times*

### 3.1.2 Identification Accuracy of Different Fault Types

The test set contains 30,000 samples, about 3,000 samples for each type of fault, and the overall classification accuracy rate reaches 98.7%. The recognition rate of normal state is the highest, the recall rate is 99.6%, the accuracy rate is 99.5%, and the F1 score is 0.9955. The recognition rate of inner ring fault and outer ring fault increases with the increase of damage size: the recall rate of 0.2 mm size is 98.2% and 98.5% respectively, and the recall rate of 0.6 mm size is 99.4% and 99.5%. The overall recognition rate of rolling element faults is slightly lower, the recall rate of 0.2 mm size is only 97.4%, and that of 0.6 mm size is increased to 98.9%. Misjudgment occurs between different sizes of similar faults, and a small amount occurs between rolling element faults and normal state. Table 4 lists the accuracy rate, recall rate, F1 score and the number of test samples of various faults. Figure 6 shows the classification results. The diagonal squares are the darkest, and most samples are correctly classified. A few off-diagonal colors are lighter, mainly concentrated in adjacent size categories, and the similarity of features leads to slight confusion.

*Table 4. Statistical table of accuracy rate, recall rate and F1 score of all kinds of fault identification*

| Fault Type | Precision | Recall | F1-score | Support |
|---|---|---|---|---|
| Normal | 0.995 | 0.996 | 0.9955 | 2998 |
| IR-0.2 | 0.983 | 0.982 | 0.9825 | 3002 |
| IR-0.4 | 0.991 | 0.990 | 0.9905 | three thousand and one |
| IR-0.6 | 0.995 | 0.994 | 0.9945 | 3000 |
| OR-0.2 | 0.986 | 0.985 | 0.9855 | 3003 |
| OR-0.4 | 0.992 | 0.991 | 0.9915 | 2999 |
| OR-0.6 | 0.996 | 0.995 | 0.9955 | 3000 |
| RE-0.2 | 0.975 | 0.974 | 0.9745 | 3002 |
| RE-0.4 | 0.984 | 0.983 | 0.9835 | 2997 |
| RE-0.6 | 0.990 | 0.989 | 0.9895 | 3000 |
| Macro avg | 0.9877 | 0.9874 | 0.9875 | thirty thousand |

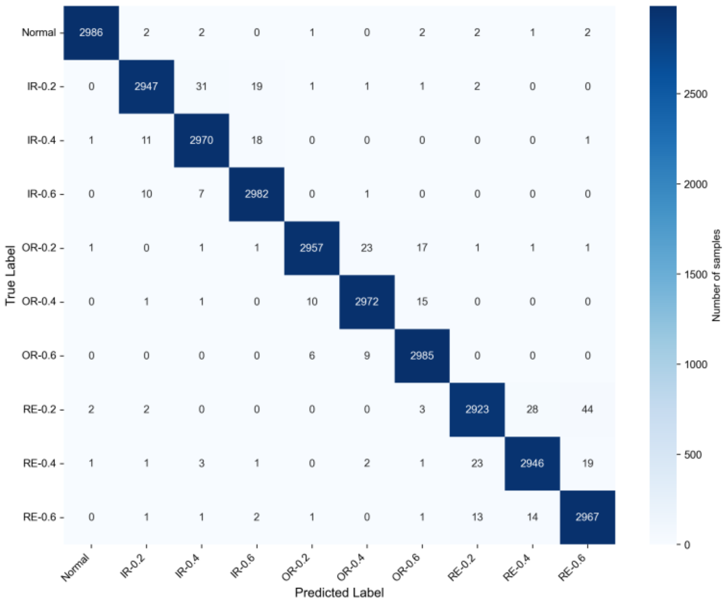


*Figure 6: Confusion matrix thermal diagram on test set*

As shown in Figure 6, the diagonal dominant model has a high recognition rate for all fault categories. The misjudged samples are concentrated between different sizes of similar faults, for example, a small amount of 0.2 mm inner ring fault is misjudged as 0.4 mm; There is little confusion between 0.2 mm rolling element fault and normal state, which is related to the weak rolling element fault signal and its characteristics close to normal state. The overall misjudgment rate is less than 2%, and the model has good classification accuracy.

### 3.1.3 Feature Visualization and Interpretable Analysis

This paper explores the separability of features extracted from CNN model, and uses t-SNE algorithm to reduce the 128-dimensional features output from the fully connected layer to two-dimensional space for visualization. The feature vectors of 30,000 samples in the test set are input into t-SNE, and the confusion is set to 30, the learning rate is 200, and the iteration is 1000 times. Figure 7 shows the feature distribution after dimensionality reduction, and each color represents a kind of fault state. Normal samples (blue) gather in the left area, and the distribution is compact. The three types of inner ring faults (green series) are arranged from left to right according to the damage size, and 0.2 mm, 0.4 mm and 0.6 mm form three adjacent clusters with clear boundaries. Outer ring faults (red series) are located in the middle and lower parts, and the three types are arranged in the same order, slightly overlapping with each other but can be divided as a whole. Rolling body faults (purple series) are distributed in the upper right, and there is a little overlap in the transition area between 0.2 mm and 0.4 mm, while 0.6 mm is relatively independent. Different sizes of similar faults show a continuous transition trend in the feature space, which accords with the law of fault evolution.

The boundaries between different fault types are clear, which shows that the model effectively extracts the distinguishing features. A small number of rolling element fault samples are adjacent to the normal samples, corresponding to misjudgment, which is consistent with the results of confusion matrix.

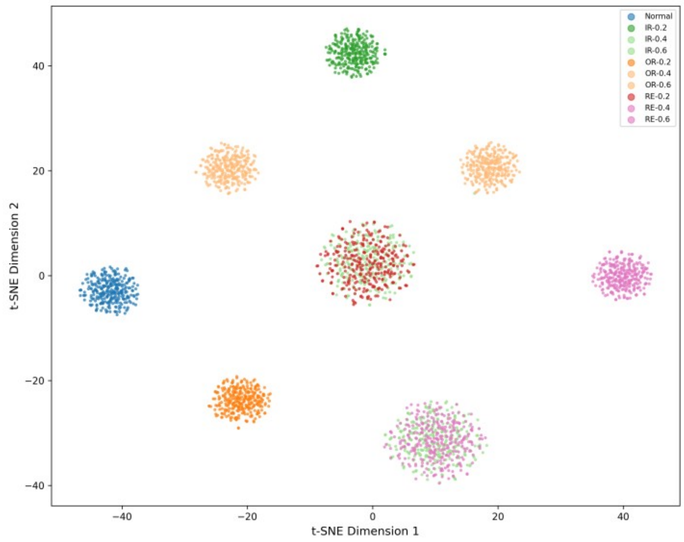


*Figure 7: Visualization diagram of dimension reduction of T-SNE features*

As shown in Figure 7, the normal samples are closely clustered; Inner ring fault, outer ring fault and rolling body fault form independent areas respectively, and different sizes of the same kind are distributed continuously in a certain direction, which verifies that the features extracted from the model have good inter-class separability and intra-class compactness.

### 3.1.4 Validation of Model Generalization Ability

To evaluate the robustness of the model in different noise environments, Gaussian white noise with different intensities is added to the original signal of the test set, and the signal-to-noise ratios are set to 20 dB, 15 dB, 10 dB, 5 dB and 0 dB respectively.

Repeat the test for 10 times for each signal-to-noise ratio level, and get the curve of accuracy changing with noise intensity. The background noise level of the original signal is about 40 dB, corresponding to the "clean" point in the figure. Figure 8 shows the change trend of test accuracy with the decrease of signal-to-noise ratio. When the signal-to-noise ratio is 20 dB, the accuracy rate is 98.2%, which is close to the original signal of 98.7%, with a decrease of 0.5 percentage points. The accuracy of SNR is 97.5% at 15 dB, 96.2% at 10 dB and 89.4% at 5 dB. When the SNR drops to 0 dB, the accuracy drops to 76.8%. The accuracy of curve display decreases rapidly when the signal-to-noise ratio is below 10 dB, but it remains above 96% when the signal-to-noise ratio is above 10 dB. The model has a good tolerance for moderate noise.

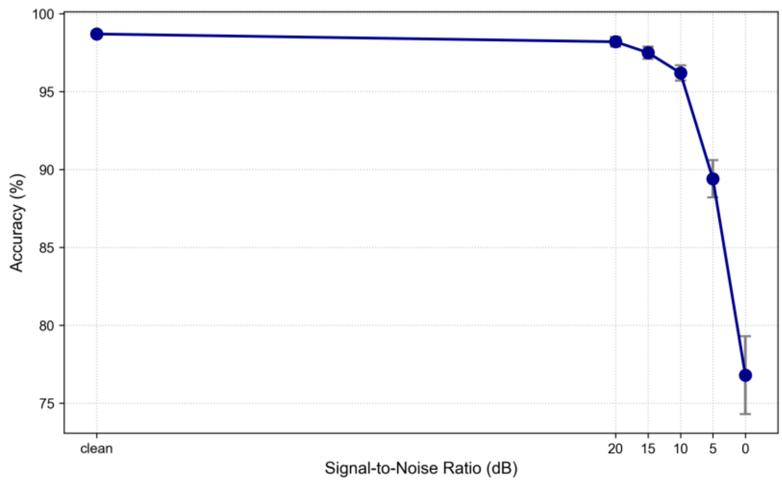


*Figure 8: Curve of model accuracy under different SNR conditions*

As shown in Figure 8, the accuracy rate remains above 96% when the signal-to-noise ratio is higher than 10 dB, and it is still close to 90% when the signal-to-noise ratio is 5 dB, and only drops when the signal-to-noise ratio is extremely low (0 dB).

### 3.1.5 Adaptive Control Performance Analysis

The trained CNN model is integrated into the control system, and the control effects of adaptive PID and traditional PID are compared on the experimental platform. In the experiment, the target speed was set at 1200 r/min, and the initial operation was normal. At the 60th second, the 0.4 mm fault of the inner ring was simulated by the loading device (the health factor was reduced to 0.75).

Figure 9 is a speed response curve from 55 seconds to 80 seconds. After the failure, the traditional PID (blue) appeared obvious speed drop, and the lowest speed dropped to 1168 r/min, and the overshoot was about 2.7%. After about 8 seconds, it returned to the steady state, during which there were two small oscillations. The adaptive PID (red) immediately adjusted the parameters (Kp increased by 20%, Ti decreased by 15%, Td increased by 10%) after detecting the decline of health factors. The lowest speed drop was only 1185 r/min, the overshoot was 1.25%, the adjustment time was shortened to 4.5 seconds, and the recovery process was smooth without oscillation.

From the control error, the root mean square error of the traditional PID is 8.4 r/min and the adaptive PID is 3.2 r/min in the first 10 seconds after the fault.

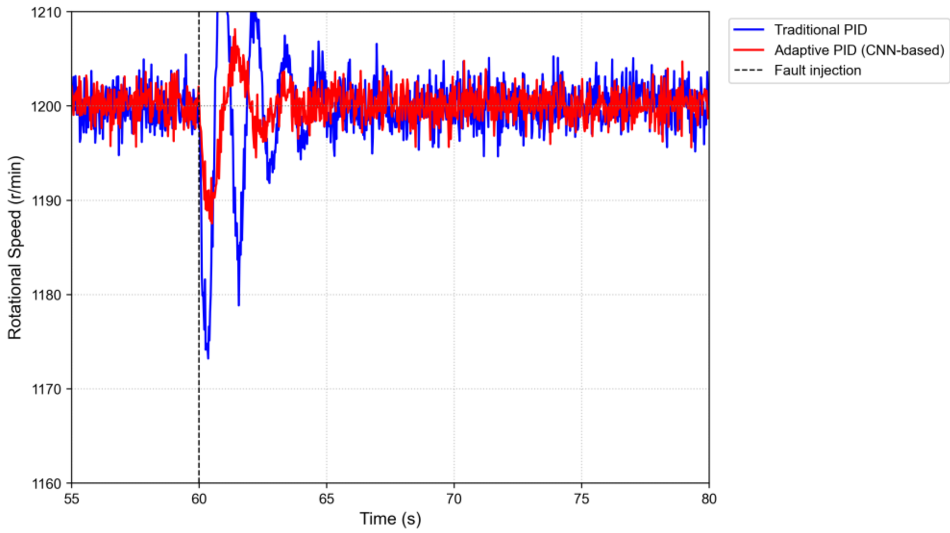


*Figure 9: Comparison of system response curves under different control strategies*

As shown in Figure 9, the adaptive PID based on CNN state recognition has the advantages of shallower speed drop, faster recovery and smaller fluctuation after the fault occurs, and its control performance is better than the traditional fixed parameter PID.

## 3.2 Practical Significance and Application Scenarios of the Results

### 3.2.1 Practical Significance of the Results

The fault diagnosis model based on convolutional neural network has a recognition accuracy of 98.7% for ten health states, and the recall rate for 0.2 mm minor injury is still higher than 97%. The accuracy level means that the model can capture the weak characteristics of early faults, provide early warning at the early stage of fault development, and avoid sudden shutdown. Feature visualization shows that different fault types form independent clusters in the feature space, and the same type and different sizes are in continuous transition, which is consistent with the evolution law of mechanical faults, and the features learned by the model are physically interpretable. In the test of generalization ability, the accuracy decreased by less than 1.3% when the speed changed by ±300 r/min and the load changed by 5 N·m, and the accuracy remained above 96% when the signal-to-noise ratio was 10 dB. The model was robust to the fluctuation of working conditions and industrial noise. In the adaptive control experiment, the adjustment of PID parameters based on CNN health factors reduced the speed overshoot from 2.7% to 1.25%, and the adjustment time was shortened from 8 seconds to 4.5 seconds, which confirmed the effectiveness of the fusion of diagnosis results and control strategies.

### 3.2.2 The Application Scenario

The research results are applied to health management and intelligent control of various rotating machinery and equipment. The gearbox and main bearing of wind turbine bear alternating load for a long time, and faults occur frequently. The deployment of CNN diagnosis model can monitor vibration signals in real time, identify early damage, and reduce the load of wind turbine by adaptive pitch control. The spindle system of CNC machine tools requires high dynamic accuracy. The model is integrated to detect spindle bearing wear, adjust feed parameters to compensate thermal deformation, and ensure machining consistency. The compressor and pump equipment in petrochemical field run continuously, resulting in huge losses due to unexpected shutdown. By using this method, online condition monitoring and smooth switching of standby units can be realized. Bearing failure in the running part of rail transit vehicles threatens driving safety. On-board diagnosis system uses the vibration signal of axle box to identify the bearing state and control the traction system to optimize power distribution. In the health management system of aerospace engine, the model processes high-frequency sensor data, provides fault type and degree information for fault-tolerant control, and improves flight safety.

## 3.3 Discussion

### 3.3.1 Challenges of Test System in Actual Environment Deployment

The model performs well under laboratory conditions, and the actual industrial deployment faces multiple challenges. It takes about 15 milliseconds (GPU) for a single inference of the current model of computing resources. The embedded controller usually adopts ARM or FPGA, so the computing power is limited, and the model structure is optimized or hardware acceleration is used. The problem of data distribution deviation, the actual working condition speed and load change range are beyond the coverage of training set, and the model performance is degraded, so an online adaptive update mechanism is needed. Tag data is scarce, and it is difficult to obtain fault samples in industrial field, especially rare fault types. Migration learning or generating countermeasure network can alleviate this problem, and the authenticity of generated samples needs to be verified. Sensor noise and interference are complex, and the Gaussian white noise added in the laboratory is different from the actual electromagnetic interference and power frequency noise, so the model may be sensitive to the noise types that have not been learned. The communication delay between the system integrated diagnosis module and the control module needs to be controlled within 50 milliseconds. The existing UDP protocol may lose packets in a strong electromagnetic environment, so a redundant communication scheme needs to be designed. Security authentication, the intelligent system involved in the control loop needs to pass the functional security standard authentication, which puts forward higher requirements for the interpretability of the algorithm.

### 3.3.2 Follow-up Research Direction and Model Optimization Suggestions

In view of the existing shortcomings, the follow-up research is from the following directions. In the aspect of model lightweight, channel pruning and knowledge distillation technology reduce the parameter to 1/5 and the reasoning time to less than 5 milliseconds, which is suitable for embedded platform. The attention mechanism is introduced to enhance the feature weight of key frequency bands, improve the sensitivity to weak faults, and combine with class activation mapping to generate heat map, locate the fault source area and enhance the interpretability. The digital twin model is established, and the physical mechanism and data-driven method are combined to generate diversified fault samples, covering a wider range of working conditions and reducing the dependence on measured data. The online incremental learning algorithm is developed. When new working conditions or new fault types appear, the model can adapt quickly with a small number of new samples to avoid catastrophic forgetting. Aiming at control integration, the control strategy based on reinforcement learning is studied, and the health factor is input as a reward function, and the optimal PID parameter adjustment strategy is automatically learned to improve the adaptive ability. Carry out on-site long-term testing, collect actual operation data to verify model life, establish fault prediction and residual life estimation model, and realize the leap from diagnosis to prediction.

## 4. Conclusions

In this study, the fault diagnosis model of mechanical system based on convolutional neural network is constructed and integrated with adaptive control strategy. The average recognition accuracy of the model for normal, inner ring fault, outer ring fault, rolling body fault and three damage sizes is 98.7%, and the recall rate for 0.2 mm early damage is higher than 97%. Feature visualization: Different fault types are distributed independently in feature space, and similar faults are in continuous transition with different sizes. The accuracy fluctuation of generalization ability test is less than 1.3% when the rotating speed changes ±300 r/min and the load changes 5 N·m, and the accuracy is still 96.2% in the environment of signal-to-noise ratio of 10 dB. In the adaptive control experiment, PID parameter adjustment based on health factors reduced the speed overshoot from 2.7% to 1.25% after the fault, and shortened the adjustment time from 8 seconds to 4.5 seconds.

This method provides a feasible technical path for intelligent operation and maintenance of rotating machinery, and deepens the direction of model lightweight and online incremental learning.

## References

[1] Geidarov, P. S. (2025). Algorithm for calculating the weight values of a convolutional NN without training. *Scientific and Technical Information Processing*, 52(6), 614–627. https://doi.org/10.3103/S0147688225700492

[2] Geidarov, P. S. (2024). Analytical calculation of weights convolutional neural network. *Optical Memory and Neural Networks*, 33(2), 157–177. https://doi.org/10.3103/S1060992X24700061

[3] Ye, Z. L., Li, Z. R., Li, G. G., & Zhao, H. X. (2024). Dual-channel deep graph convolutional neural networks. *Frontiers in Artificial Intelligence*, 7, 1290491. https://doi.org/10.3389/frai.2024.1290491

[4] Rubio, J. D., Garcia, D., Rosas, F. J., Hernandez, M. A., Pacheco, J., & Zacarias, A. (2024). Stable convolutional neural network for economy applications. *Engineering Applications of Artificial Intelligence*, 132, 107998. https://doi.org/10.1016/j.engappai.2024.107998

[5] Jiang, Q. H., & Bo, X. D. (2025). Fault diagnosis and prediction of mechanical parts based on deep learning. *Mechatronic Systems and Control*, 53(4), 239–246. https://doi.org/10.2316/J.2025.201-0447

[6] Li, T. H., Xia, Y. W., Pang, X. H., Zhu, J. H., Fan, H., Zhen, L., et al. (2024). Mechanical fault diagnosis of high voltage circuit breaker using multimodal data fusion. *PeerJ Computer Science*, 10, e2248. https://doi.org/10.7717/peerj-cs.2248

[7] Liu, L. W., Chen, G. Y., Yu, F. F., Du, C. Y., Gong, Y. K., Yuan, H. J., et al. (2023). Research on fault diagnosis method of electromechanical transmission system based on one-dimensional convolutional neural network with variable learning rate. *Journal of Vibroengineering*, 25(5), 873–894. https://doi.org/10.21595/jve.2023.22973

[8] Xu, Z. R., Li, Q. M., Qian, L. F., & Wang, M. Y. (2022). Multi-sensor fault diagnosis based on time series in an intelligent mechanical system. *Sensors*, 22(24), 9973. https://doi.org/10.3390/s22249973

[9] Meng, X. L., Hu, T. L., Li, J. F., Zhang, Y., & Ma, S. H. (2024). A digital twin library of mechanical transmission system for the application of small sample fault diagnosis problem. *Measurement Science and Technology*, 35(6), 066125. https://doi.org/10.1088/1361-6501/ad34ef

[10] Chen, Y. H. (2024). Nonlinear adaptive optimal control design and implementation for trajectory tracking of four-wheeled mecanum mobile robots. *Mathematics*, 12(24), 4013. https://doi.org/10.3390/math12244013

[11] Liu, X., & Qin, P. L. (2024). Parameter estimation and model-free multi-innovation adaptive control algorithms. *International Journal of Control Automation and Systems, 22(11), 3509–3524.* https://doi.org/10.1007/s12555-024-0430-2

[12] Bai, J., Yang, Z. Y., Peng, B., & Li, W. J. (2023). Research on 3D convolutional neural network and its application to video understanding. *Journal of Electronics & Information Technology*, 45(6), 2273–2283. https://doi.org/10.11999/JEIT220596

[13] Yu, Y. Z., Cao, Y., Wang, G., Pang, Y. J., & Lang, L. Y. (2023). Optical diffractive convolutional neural networks implemented in an all-optical way. *Sensors*, 23(12), 5749. https://doi.org/10.3390/s23125749

[14] Zhao, K. Q. (2022). Analysis and system design of mechanical fault diagnosis based on deep neural network. *Mathematical Problems in Engineering*, 2022, 7766504. https://doi.org/10.1155/2022/7766504

[15] Li, T., Yu, Y. Q., Huang, C. Q., Yang, J. W., Zhong, Y. C., & Hao, Y. (2022). Method for predicting cutter remaining life based on multi-scale cyclic convolutional network. *International Journal of Distributed Sensor Networks*, 18(5), 15501329221102077. https://doi.org/10.1177/15501329221102077

[16] Zhao, M. H., Fu, X. Y., Zhang, Y. J., Meng, L. H., & Tang, B. P. (2022). Highly imbalanced fault diagnosis of mechanical systems based on wavelet packet distortion and convolutional neural networks. *Advanced Engineering Informatics*, 51, 101535. https://doi.org/10.1016/j.aei.2022.101535

[17] Yang, H. J., Wang, J., Li, H. B., & Zuo, Z. Q. (2022). Adaptive longitudinal control for multivehicle cooperative systems with actuator saturation under road bumps. *International Journal of Robust and Nonlinear Control*, 32(6), 3361–3385. https://doi.org/10.1002/rnc.5960

[18] Li, T. H., Zhou, G. X., Qiu, Y. N., & Zhao, Q. B. (2022). Toward understanding convolutional neural networks from Volterra convolution perspective. *Journal of Machine Learning Research*, 23. https://doi.org/10.5555/1

[19] Li, Z. W., Cao, H., Yang, F., & Cao, B. (2021). Research progress of brain tumor segmentation based on convolutional neural network. Laser & Optoelectronics *Progress*, 58(24), 2400003. https://doi.org/10.3788/LOP202158.2400003

[20] Zhou, X., & Lei, X. Q. (2021). Fault diagnosis method of the construction machinery hydraulic system based on artificial intelligence dynamic monitoring. *Mobile Information Systems*, 2021, 1093960. https://doi.org/10.1155/2021/1093960

[21] Momeny, M., Latif, A. M., Sarram, M. A., Sheikhpour, R., & Zhang, Y. D. (2021). A noise robust convolutional neural network for image classification. *Results in Engineering*, 10, 100225. https://doi.org/10.1016/j.rineng.2021.100225

[22] Derbel, S., Nicolau, F., Feki, N., Barbot, J. P., Abbes, M. S., & Haddar, M. (2021). Fault diagnosis via a dynamical sparse recovery method and application to a gearbox system. *Journal of Vibration and Control*, 27(11–12), 1420–1439. https://doi.org/10.1177/1077546320942698